Wiley
International Journal of RF and Microwave Computer-Aided Engineering
Volume 2026, Article ID 3937372, 13 pages
https://doi.org/10.1155/mmce/3937372

WILEY

Research Article

Uniform Circular Array Antenna for Dual-Mode Orbital Angular Momentum Generation at 6 GHz

Abdulkadir Uzun [1] **and Ibrahim Tekin** [1,2]

[1]*Electronics Engineering, Sabanci University, Istanbul, Turkey*
[2]*Sabanci University Nanotechnology Research and Application Center, Istanbul, Turkey*

Correspondence should be addressed to Abdulkadir Uzun; kadiruzun@sabanciuniv.edu

Received 30 July 2025; Revised 28 October 2025; Accepted 17 November 2025

Academic Editor: Piotr Gas

Orbital angular momentum (OAM) antennas have recently attracted attention for their potential to enhance communication capacity and and robustness against interference. However, most existing designs rely on complex multilayer feed structures. This work presents a compact, single-layer, series-fed dual-mode OAM antenna composed of four patches arranged in a circular array with a 29 mm radius. The series-feeding network can be excited from two ports to simultaneously generate the $l = +1$ and $l = -1$ modes. Measurements were performed in an anechoic chamber to obtain far-field realized gain patterns and holographic phase distributions in the 6 GHz band. Two identical antennas were also tested in a transmit–receive configuration in a multipath environment using a two-port vector network analyzer. The maximum realized gains are 3.65 dBi for $l = +1$ and 4.8 dBi for $l = -1$ at 6.1 GHz. The proposed single-layer topology enables dual-mode OAM generation and supports multimode multiplexing, enhancing spectral efficiency and suppressing interference without added hardware complexity.

Keywords: dual-mode; orbital angular momentum; series-fed array; uniform circular array; vortex beam

1. Introduction

OAM is a physical layer multiplexing method characterized by two key properties: the orthogonality of different modes and beam divergence. Orthogonality can be leveraged for multiplexing and to enhance capacity and spectrum efficiency in communication systems [1], whereas beam divergence may replace conical scanning antennas in the future and be used for radio frequency systems such as satellite communication antennas on vehicles [2, 3]. Owing to the OAM properties, the International Telecommunication Union Radiocommunication Sector (ITU-R) Working Party 5D (WP 5D), which is responsible for terrestrial radio systems of International Mobile Telecommunications (IMT), has framed OAM as one of the potential technologies for IMT-2030 systems, aka 6G [4].

The foundation of OAM's unique characteristics can be traced back to 1992, when Allen et al. first demonstrated that an OAM beam possesses a spiral wave front which is characterized by an additional phase term $e^{il\phi}$ (i imaginary unit, l OAM mode number, ϕ azimuth angle) [5]. The phase term of the spiral wave front ranges from 0 to $2\pi l$ in a full turn, with the number of modes defined by the number of wave front twists occurring over a propagation distance equal to one wavelength. Recent reviews on various OAM antennas highlight the critical need for simpler feeding networks for future wireless communication applications [6–8]. To address this, we develop a novel feed technique for uniform circular array antennas (UCAA), to reduce both the cost and profile. The simulation and design of the single-layer dual-mode OAM antenna were presented in our previous work [9]. In the paper, we proposed series-feeding network for the design of OAM generating UCAA that can be applied to different polarization and frequency bands to create multimode OAM antennas, instead of UCAA designs that either support single polarization or require complex feeding networks [10, 11], multiple concentric UCAAs [12], or multilayer structures [13] to achieve dual-polarization, dual-

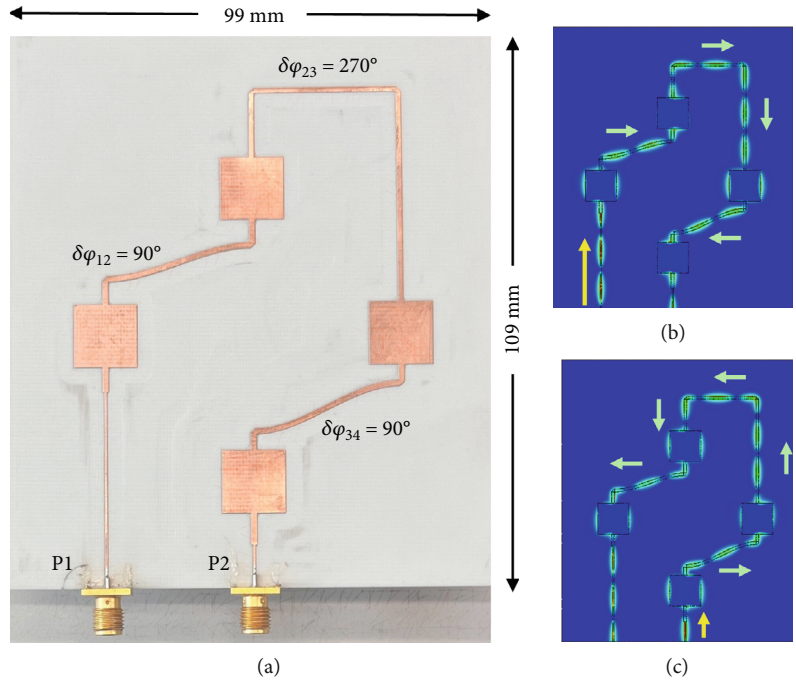

FIGURE 1: Single-layer dual-mode OAM antenna: (a) implementation ($\delta\varphi_{ab}$ represents the interelement phase differences between the a^{th} and b^{th} elements), (b) current flow for $l = +1$, and (c) current flow for $l = -1$.

TABLE 1: Design properties of the UCA-based dual-mode OAM antenna.

Antenna property	Value
Array radius	29 mm
Port number	2 ports
Dimensions	$99 \times 109 \times 0.813$ mm^3
OAM modes (l)	±1
Polarization	Linear
Element number	4
Interelement phase difference	90° (270° if element is inverted)
Substrate material	Rogers RO4350B

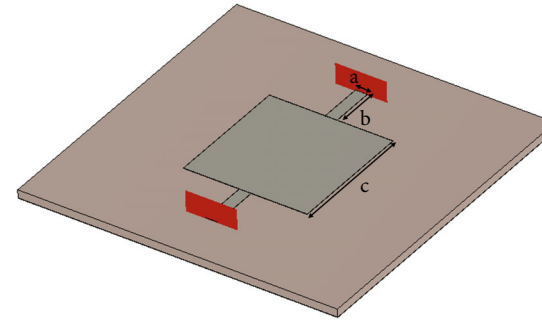

FIGURE 2: Design of a single patch unit cell for S-parameters of a square radiating element.

TABLE 2: ABCD parameters of the unit cell at 6.1 GHz.

A	B	C	D
$0.474 - 0.069j$	$7.648 - 68.01j$	$-0.0004 - 0.0112j$	$0.508 - 0.055j$

band, and multimode OAM generation. Recent OAM antenna studies reveal clear trade-offs between reconfigurability, aperture size, and design simplicity. Rao et al. [14] enabled three modes ($l = 0, \pm 1$) at 6 GHz with PIN-diode switching, but with higher circuit complexity. A simpler approach was shown by Vedaee and Mallahzadeh [15], who used a single-layer SIW slot array for two modes ($l = 0, +1$) with moderate gain. For long-range links, Habibi Daronkola et al. [16] employed concentric UCAs to form quasi-OAM superpositions, improving directivity at the cost of larger apertures. Compact alternatives include Li et al. [13] with a dual-polarized four-element array at 5.5 GHz and Rao et al. [17] with a 6 GHz UCA producing $l = -1$. Distinct from these efforts, the proposed antenna achieves dual-mode OAM ($l = \pm 1$) at 6 GHz with only four elements in a single-layer PCB, offering a uniquely compact and fabrication-friendly solution without the need for multilayer structures, large apertures, or active switching.

Figure 1a presents the fabricated dual-mode OAM antenna and interelement phase differences. In Figure 1b,c, we showed the current flow that corresponds to OAM modes $l = +1$ and $l = -1$, respectively.

In this paper, we aim to characterize the implemented series-fed, single-layer, dual-mode OAM antenna using anechoic chamber and in-lab measurements to demonstrate its dual-mode OAM capabilities. We also aim to show that

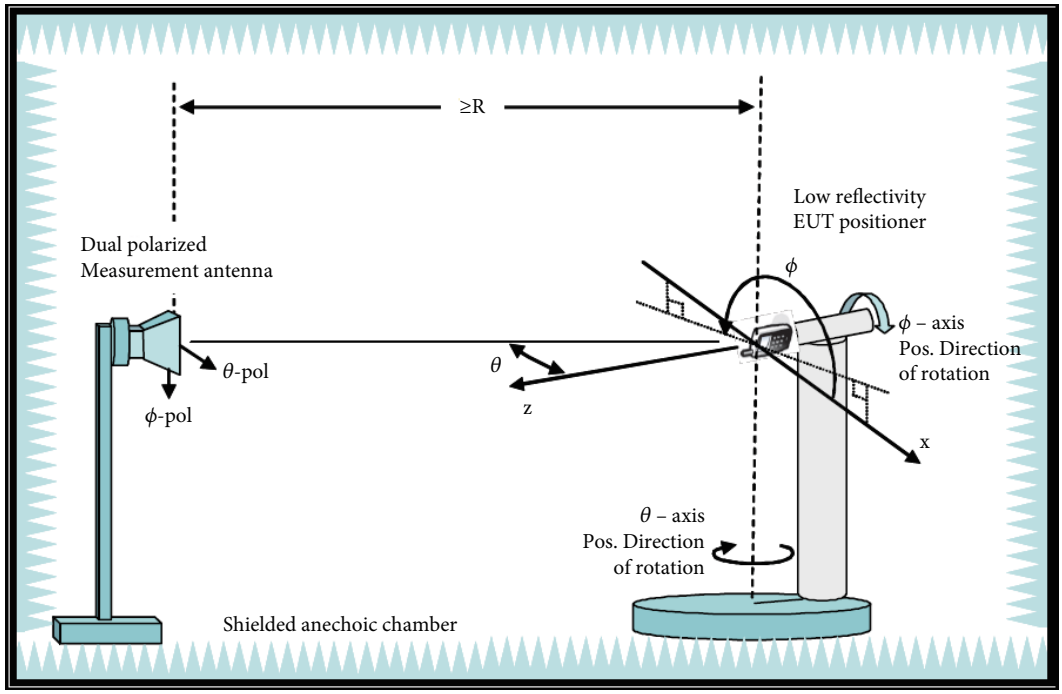

FIGURE 3: Anechoic chamber distributed axis system [19].

the designed and implemented single-layer UCAA and its novel feeding network is capable of generating dual OAM modes ($l = \pm 1$). Eventually, this novel feeding approach may lead to easier deployment of OAM multiplexing antennas and can be generalized for multimode dual-polarized OAM antennas.

This paper is structured as follows: Section 2 details the antenna and feed network design, Section 3 provides an overview of the measurement setups, Section 4 details the measurement results, and Section 5 offers concluding insights.

2. Antenna Design

This section outlines the design of the proposed antenna, structured in two parts: the geometry of the uniform circular array (UCA) and the synthesis and refinement of the series feed network.

2.1. UCA Design. The proposed antenna system, illustrated in Figure 1a, is a UCA specifically designed for orbital angular momentum generation. It consists of four microstrip elements implemented on a single substrate and optimized through full-wave simulations. In this design, the feeding network ensures equal power distribution among all elements. To realize OAM radiation, a cumulative phase progression of $2\pi l$ is introduced between the first and last array elements, achieved through carefully engineered interelement connections. As a result, each successive element is excited with a phase increment ($\delta\varphi$) of $2\pi l/N$, where N is the total number of elements in the array. It is well established that a UCA with N elements can generate OAM modes are bounded by $N/2 < l < N/2$.

In this work, a four-element configuration is employed, enabling the generation of vortex beams with mode numbers $l = \pm 1$. The required 90° progressive phase shift between consecutive elements is inherently embedded in the feeding structure, yielding a compact, single-layer, series-fed dual-mode OAM antenna.

UCA radius was optimized to 29 mm, ensuring proper interelement connections for accurate power division and phase progression. Due to the 180° polarization reversal between the second and third patches (counting from the ports), the interconnect line connecting these elements was lengthened to introduce an additional 180° phase delay, resulting in a total phase shift of 270°. Furthermore, the interconnect line widths were carefully optimized through rigorous analysis and simulations to achieve the desired radiation characteristics and high OAM mode purity. The design properties of the series-fed dual-mode OAM antenna are summarized in Table 1.

2.2. Series Feed Network Design. In our design, the antenna elements are series fed to create a concise and simpler design. The challenges associated with series-fed OAM have been addressed through a novel network that ensures equal power distribution and the required phase shift between consecutive elements for the generation of dual OAM modes.

The performance of the proposed series-fed patch array is determined largely by the interconnecting microstrip lines, which control both impedance matching and element excitation. To establish a design basis for the feeding network, a single square patch unit cell, as illustrated in Figure 2, was designed and simulated in CST. The design parameters a, b, and c are 1.2 mm, 4.87 mm, and 12.5 mm, respectively.

FIGURE 4: Measurement setups: (a) far-field measurement in anechoic chamber, (b) antenna side view in anechoic chamber with coordinate system, and (c) RF power transmission experiment using VNA in laboratory.

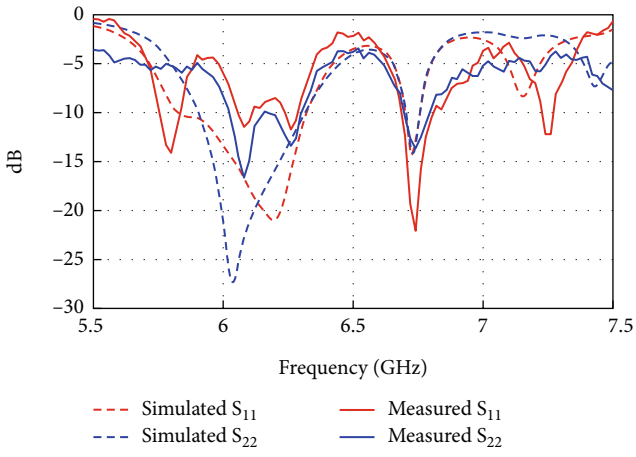

FIGURE 5: Measured (solid) and simulated (dashed) S-parameters.

After analyzing the S-parameters of the unit cell, we converted them into ABCD form (Table 2). Following the approach in [18], Bloch theory was applied to extract the Bloch impedance and phase per cell, yielding an initial design target of approximately 78.7 Ω for the interconnect microstrip lines at 6.1 GHz.

In the next stage, the feed network was refined through full-wave optimization of the finite four-element array. Because the interconnect lines incorporate bends to realize the required interelement phase progression for OAM generation, the optimum impedance profile deviates slightly from the Bloch-based target. The final optimized impedances were approximately 64 Ω, 70.4 Ω, and 64 Ω for the interconnects between Patch 1–2, Patch 2–3, and Patch 3–4, respectively. In addition, each input feed from the respective port to the unit cell was co-optimized with the interconnects to achieve precise impedance matching, yielding a characteristic impedance of 96.5 Ω.

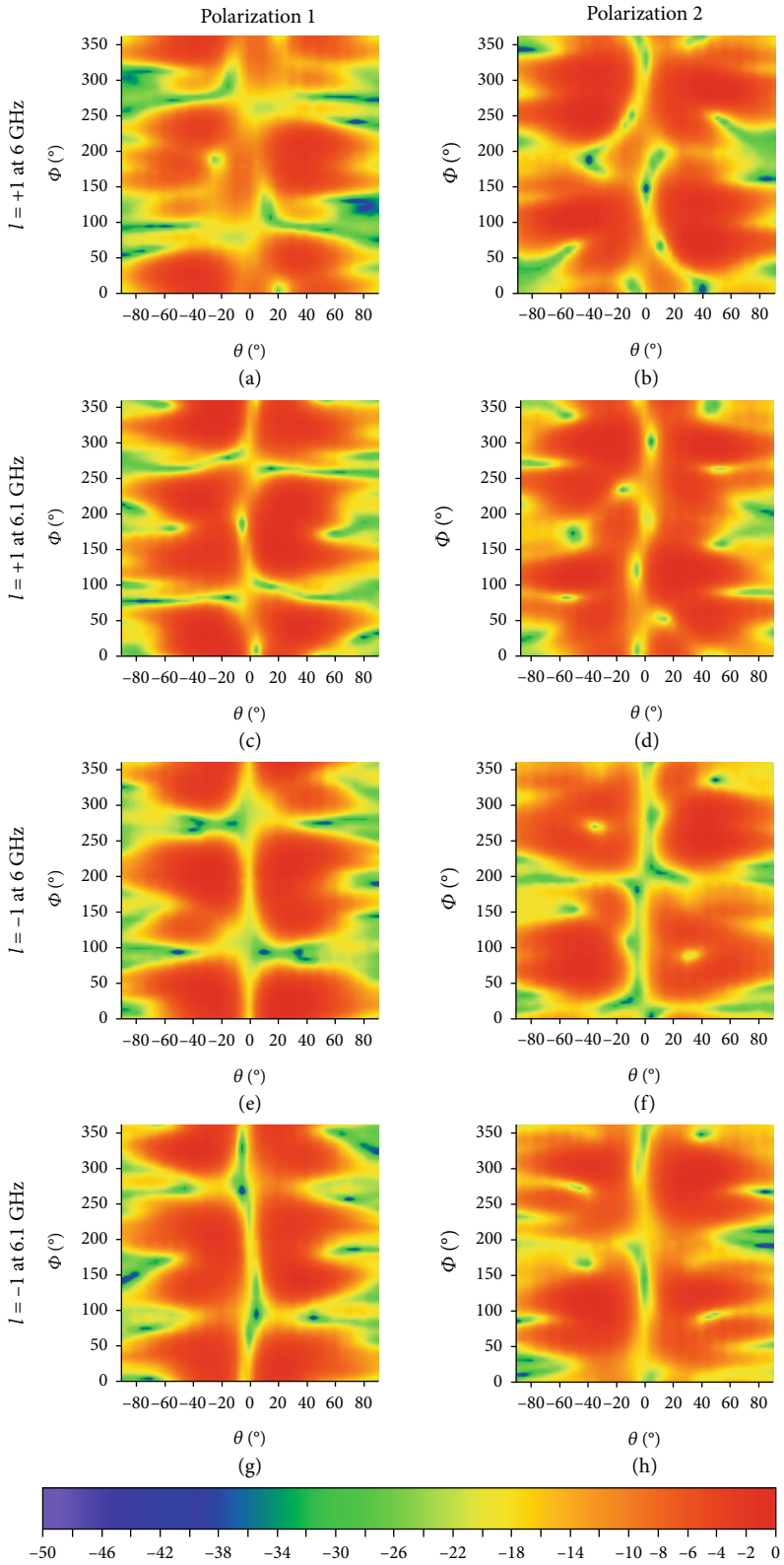

FIGURE 6: (a–h) Normalized gain plots for $0° \leq \phi \leq 360°$ and $-90° \leq \theta \leq 90°$.

3. Measurement Setups

To accurately characterize the performance of the dual-mode OAM antenna, we undertook a comprehensive measurement process which involved two distinct experimental setups. Initially, we evaluated a single OAM antenna within an anechoic chamber, to assess its S-parameters, realized far-field gain pattern, and its phase distribution. This setup

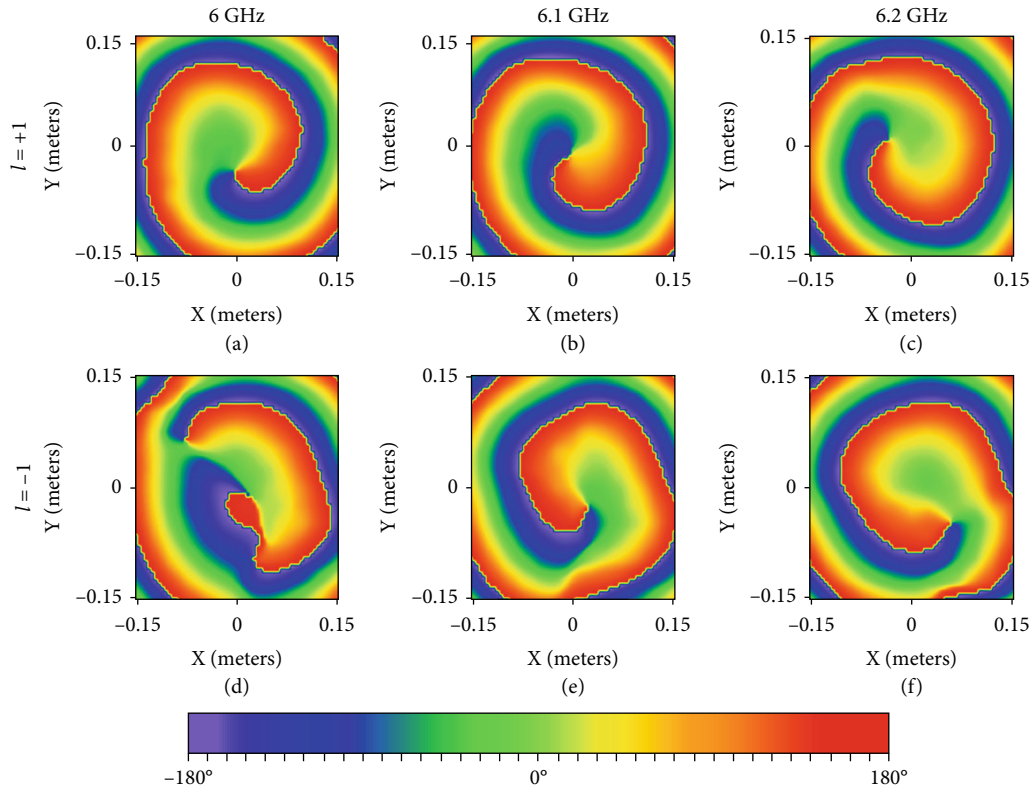

FIGURE 7: (a–f) OAM Phase Distribution.

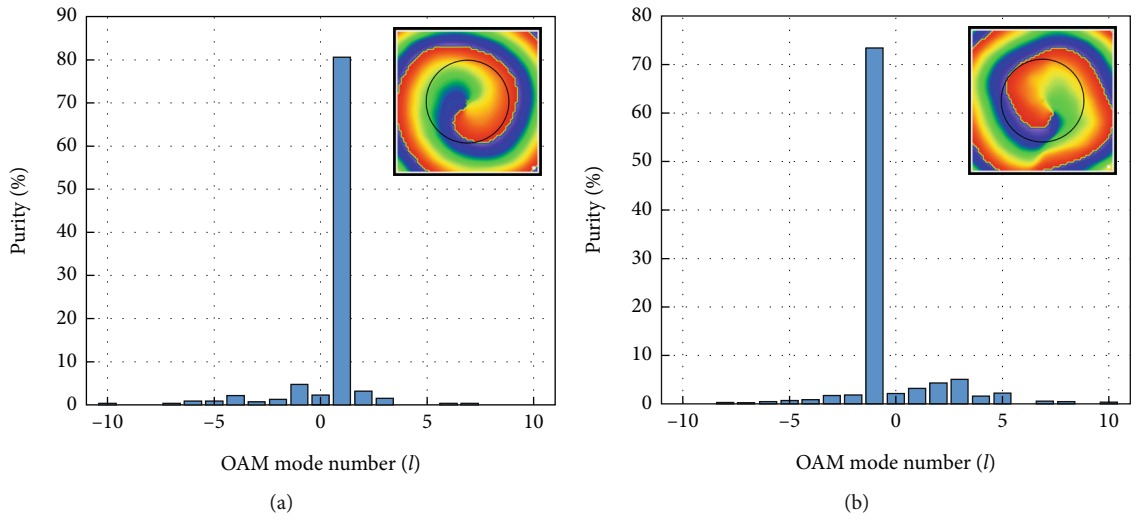

FIGURE 8: Measured OAM mode purity spectra for (a) Port 1 and (b) Port 2 excitations at 6.1 GHz.

allowed us to obtain detailed insights into the antenna's individual performance characteristics. The axis definitions of the anechoic chamber are provided in Figure 3.

The anechoic chamber measurement setup, located in Sabanci University Nanotechnology Research and Application Center (SUNUM), consists of an Agilent 2-Port and 4-Port PNA-X 250 kHz–50 GHz Network Analyzer, a SPIEL Anechoic Chamber, NSI positioner and probes, and an NSI Spherical Near Field Antenna Measurement System with an NSI Double Ridged Horn Probe Antenna. In the measurement setup, the distributed positioners in the chamber move independently through the ϕ-axis and θ-axis.

Subsequently, two identical OAM antennas were placed facing each other to measure the transmitted power levels across various modes. We utilized a two-port Rohde & Schwarz FSH4 handheld network analyzer (VNA), with one port connected to the transmitting OAM antenna and the other to the receiving OAM antenna. In this setup, we

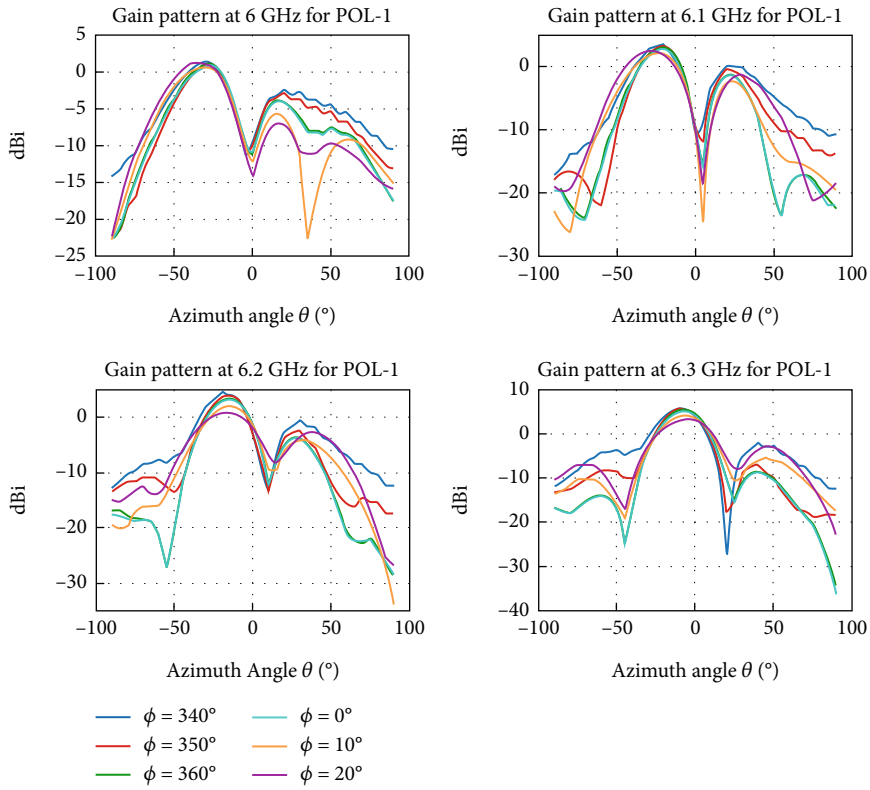

FIGURE 9: Realized gain plots for $l = +1$ and Pol-1.

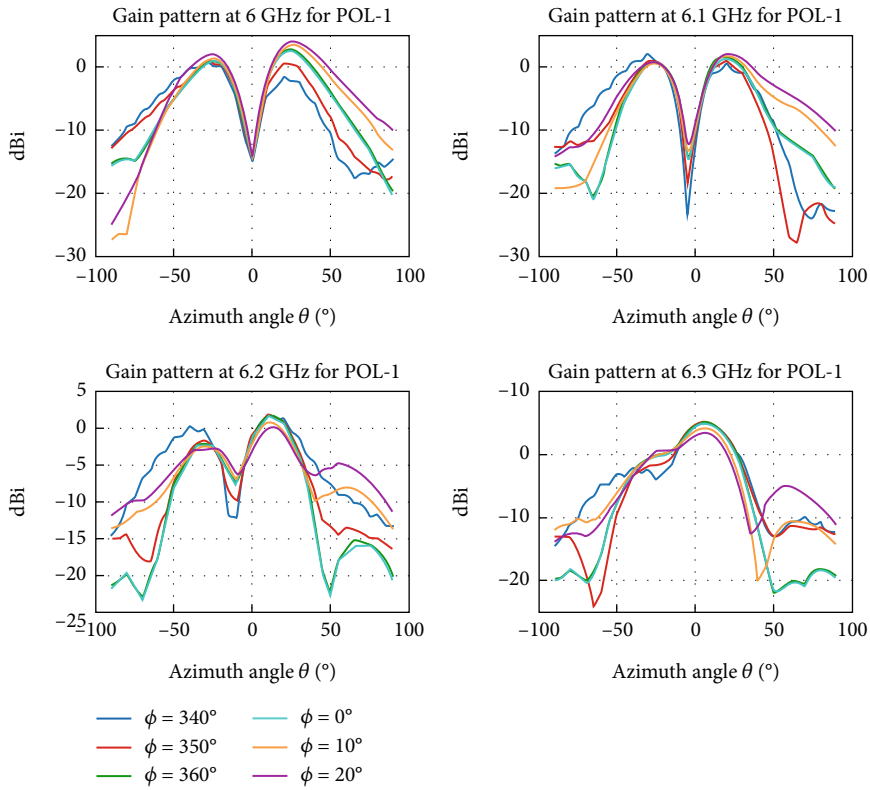

FIGURE 10: Realized gain plots for $l = -1$ and Pol-1.

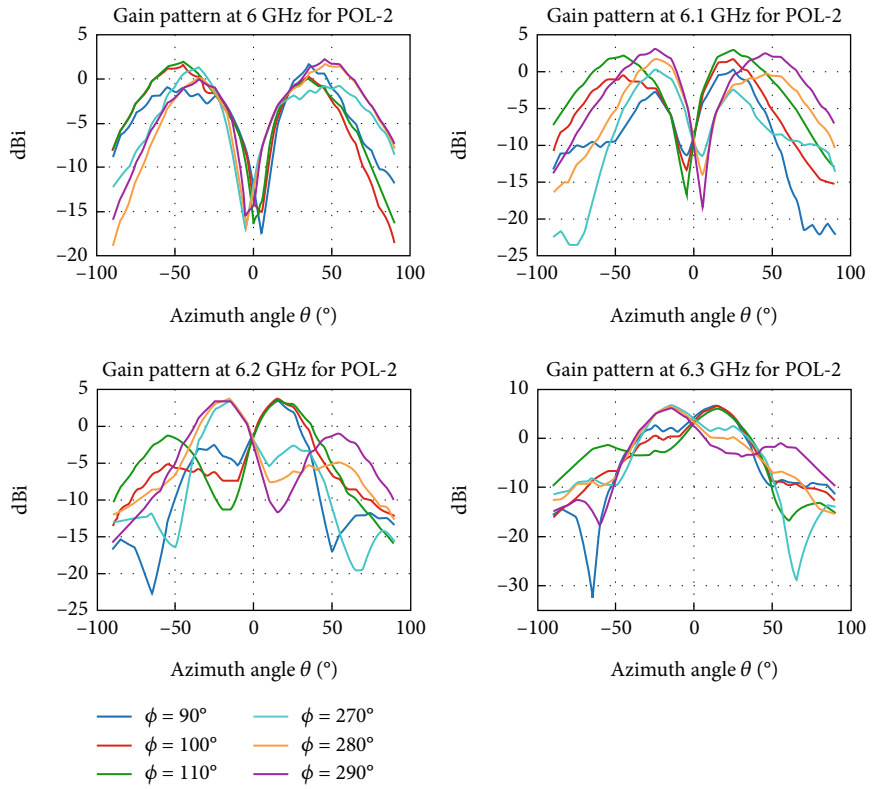

FIGURE 11: Realized gain plots for $l = +1$ and Pol-2.

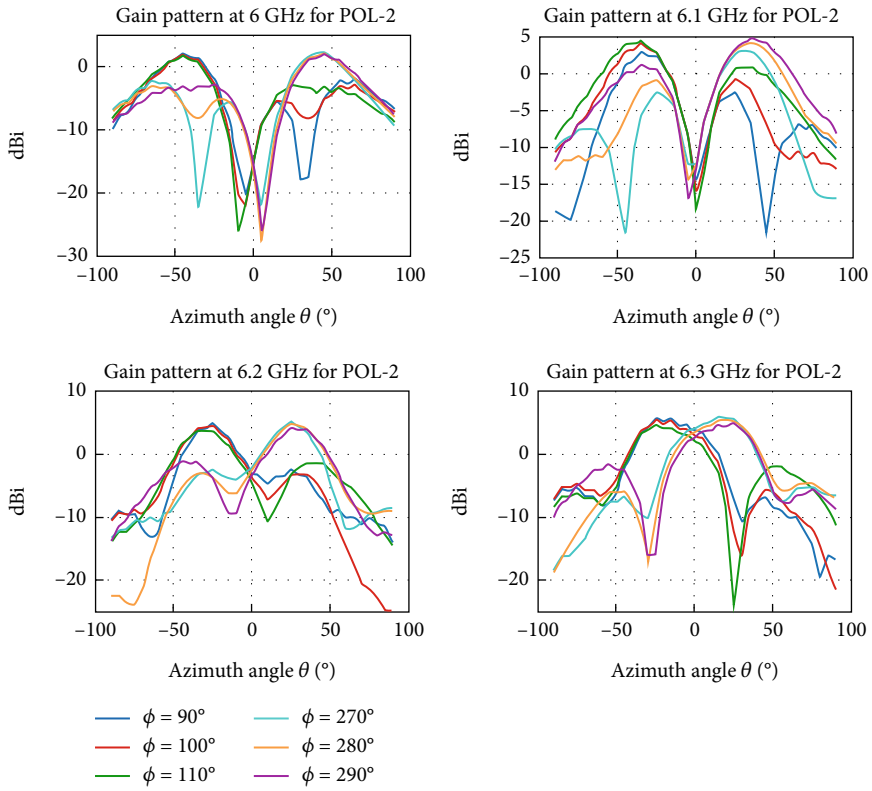

FIGURE 12: Realized gain plots for $l = -1$ and Pol-2.

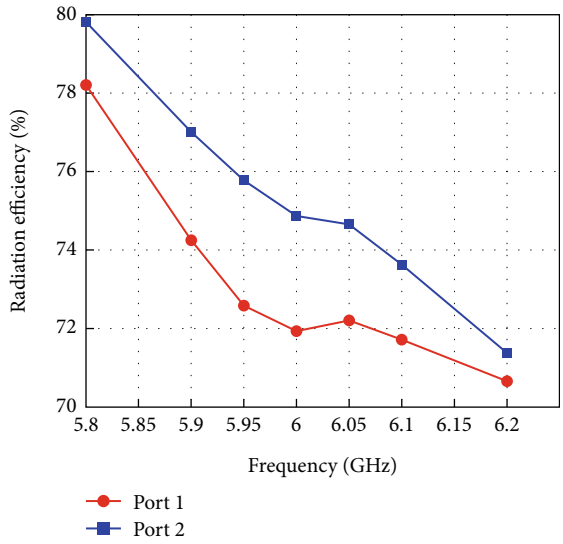

Figure 13: Simulated radiation efficiency.

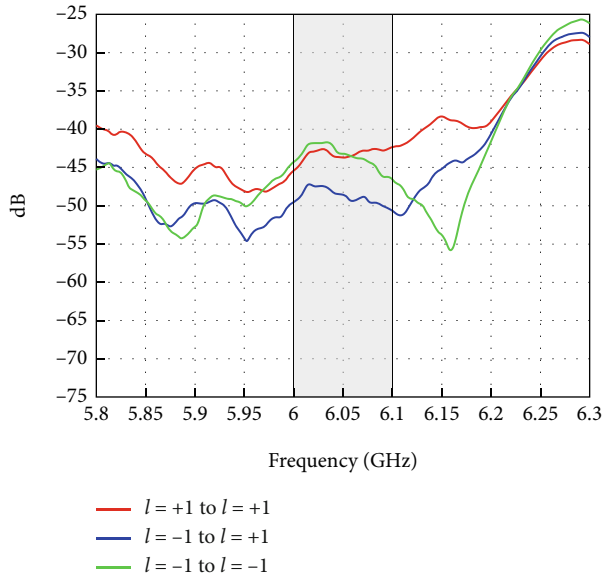

Figure 14: OAM transmission for $d = 33$ cm, $\theta = 0°$.

transmitted $l = +1$ and received $l = +1$, then transmitted $l = -1$ and received $l = -1$, and finally transmitted $l = +1$ and received $l = -1$. The first two transmissions reveal the effectiveness of the OAM transmissions, whereas the last transmission reveals the amount of cross-mode we can achieve in a multipath lab environment. Measurement setups in the anechoic chamber and in a multipath laboratory environment are depicted in Figure 4.

4. Measurement Results and Discussion

The anechoic chamber measurements presented in this section include far-field normalized radiation patterns, realized gain patterns as cuts at defined angles, and phase distributions obtained by holography. The S-parameters of the

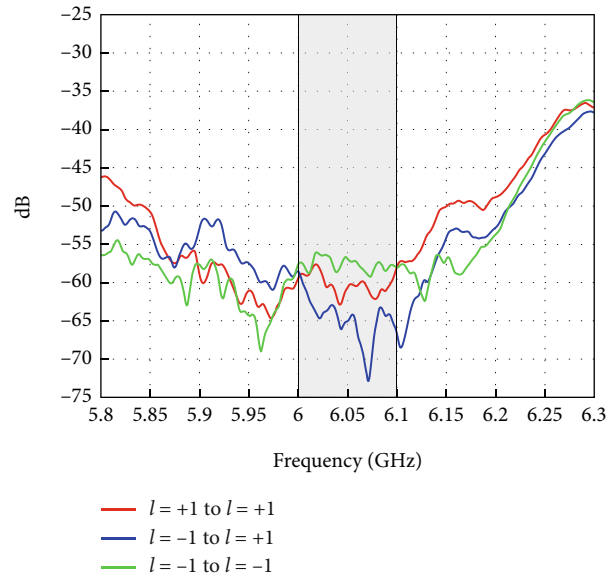

Figure 15: OAM transmission for $d = 80$ cm, $\theta = 0°$.

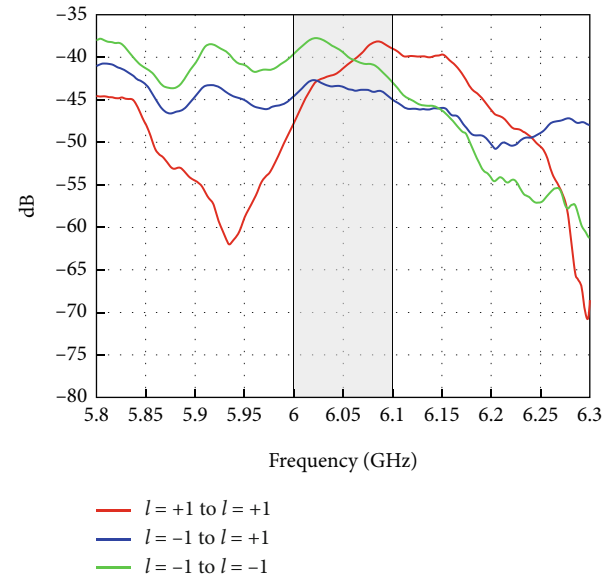

Figure 16: OAM transmission for $d = 33$ cm, $\theta = 25°$.

antenna are also provided in Figure 5, which shows that the matched frequency has shifted to the right by 100 MHz. The far-field measurement setup spans 180° in the θ-axis and 360° in the ϕ-axis. Each rotation axis has been sampled with a 5° step size, resulting in 37 points in the θ-axis and 73 points in the ϕ-axis. The measurement radius is 2.18818 m. The normalized gain plots at 6 GHz and 6.1 GHz over the measurement range, which is defined by the rotation axes as $0° \le \phi \le 360°$ and $-90° \le \theta \le 90°$, for the two orthogonal linear polarizations, Polarization 1 (ϕ-pol as in Figure 3) and Polarization 2 (θ-pol as in Figure 3), are provided in Figure 6.

When the antenna is excited from Port 1 with Port 2 terminated, a beam with OAM mode number $l = +1$ is

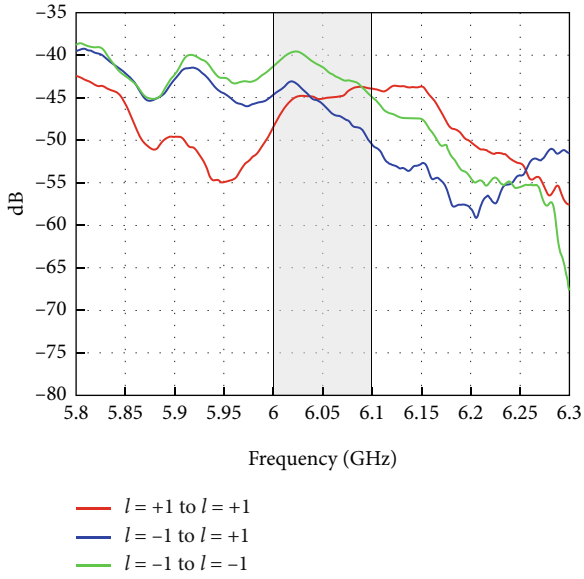

Figure 17: OAM transmission for $d = 33$ cm, $\theta = 30^{\circ}$.

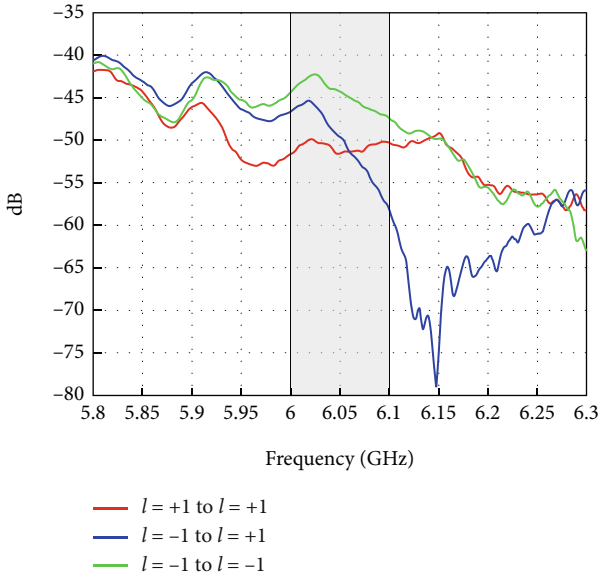

Figure 18: OAM transmission for $d = 33$ cm, $\theta = 35^{\circ}$.

generated. Its corresponding normalized gain plots, at 6 GHz and 6.1 GHz, are shown in Figures 6a, 6b, 6c, and 6d. Similarly, when the antenna is excited from Port 2 with Port 1 terminated, a beam with OAM mode number $l = -1$ is generated. Figures 6e, 6f, 6g, and 6h show normalized gain plots for $l = -1$. As for the phase distributions, they are obtained 20 cm away from the antenna using the FFT hologram algorithm in NSI 2000 software with an FFT size of 1024 by 128. The phase distributions, spanning the x-axis and y-axis by 0.3048 m, are provided in Figure 7. Furthermore, Figure 7 shows the dual-mode OAM phase distributions at frequencies 6.0 GHz (Figure 7a,d), 6.1 GHz (Figure 7b,e), and 6.2 GHz (Figure 7c,f). In this plot, the $l = +1$ mode phase distributions (Figures 7a, 7b, and 7c) seem to be purer compared to $l = -1$ (Figures 7d, 7e, and 7f), which is in line with the simulated mode purities presented in our previous work [9]. The experimental results in Figure 8 show that the dominant mode purities reach 80.6% and 73.4% for the $l = +1$ and $l = -1$ excitations, respectively, at 6.1 GHz.

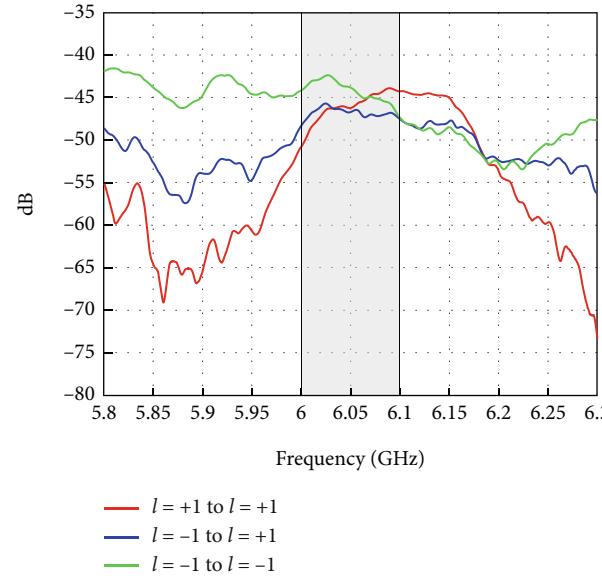

Figure 19: OAM transmission for $d = 70$ cm, $\theta = 30^{\circ}$.

The realized gain cut plots in Figures 9 and 10 represent the ϕ cuts around 0° and 360°, whereas Figures 11 and 12 show the ϕ cuts around 90° and 270°. The stacked curves in Figures 9 and 10 are plotted for cut angles of $\phi = 0^{\circ}$, $\phi = 10^{\circ}$, $\phi = 20^{\circ}$, $\phi = 340^{\circ}$, $\phi = 350^{\circ}$, and $\phi = 360^{\circ}$ since they are the patterns for Polarization-1 measurements. Similarly, the patterns for Polarization-2 measurements are plotted as stacked curves in Figures 11 and 12 at the cut angles of $\phi = 90^{\circ}$, $\phi = 100^{\circ}$, $\phi = 110^{\circ}$, $\phi = 270^{\circ}$, $\phi = 280^{\circ}$, and $\phi = 290^{\circ}$. These cut angles are determined based on the reasonable gain and null formations according to the results presented in Figure 6 for the OAM beams. There is a 90° difference between the cuts for the two polarizations because the antenna is linearly polarized; when rotated by 90° in the ϕ-axis to measure the other orthogonal polarization, the cut angle must also shift by 90°.

For $l = +1$, the maximum realized gains are 5.8 dBi at 5.8 GHz, 3.75 dBi at 5.9 GHz, 2.15 dBi at 6.0 GHz, 3.65 dBi at 6.1 GHz, 4.4 dBi at 6.2 GHz, and 6.6 dBi at 6.3 GHz. For $l = -1$, the maximum realized gains are 3.6 dBi at 5.8 GHz, 3.47 dBi at 5.9 GHz, 4.17 dBi at 6.0 GHz, 4.8 dBi at 6.1 GHz, 4.83 dBi at 6.2 GHz, and 5.9 dBi at 6.3 GHz. However, the null, which is the signature of the OAM, has been maintained between frequencies 5.8 GHz to 6.2 GHz. Therefore, the antenna is capable of generating OAM beams in the range of 5.9 GHz to 6.2 GHz. Due to S-parameter and matching of the ports, its performance is more efficient for the range of 6.0–6.2 GHz.

The simulated antenna efficiencies for Port 1 and Port 2 are shown in Figure 13. Across the 5.8–6.2 GHz band, Port 1 achieves efficiencies between 70.7% and 78.2%

TABLE 3: Comparison of OAM antenna designs in the literature and the proposed dual-mode OAM antenna.

Reference	Frequency (GHz)	Element number	OAM mode number	Gain (dBi)	Size (mm^2)	Height (mm)	Layers	Divergence angle	Complexity
[13]	5.5	4	−1 +1	9.5 10.2	120 × 112	5.3	2 (+Reflector)	28° 26°	High (3D structure)
[14]	6.0	2 + 8	0 ±1	8 10	—	1.0	1 (+Bias)	—	High (PIN diodes)
[15]	10.19	4 + 8	+1	2.3	170 × 170	0.813	1	O° 6.8°	Medium (SIW TW)
[16]	10.0	9 + 10+11	+2, +3, +4	—	140 × 140	0.8	1	N/A	High (concentric arrays)
[17]	6.0	8	−1	10.5	—	1.6	1	22°	Low (series feed)
Proposed	6.0	4	−1 +1	4.8 3.65	99 × 109	0.813	1	≈25° ≈25°	Low (series feed)

(mean ≈ 73.1%), whereas Port 2 maintains a slightly higher range of 71.4%–79.8% (mean ≈ 75.3%).

The in-lab measurements, where there are multipath conditions due to nearby walls and objects, we aim to show how identical OAM antennas facing each other transmit and receive the same OAM modes as well as different OAM modes. The antennas are placed as shown in Figure 4c. We have conducted several experiments and plotted the resulting graphs, illustrated in Figures 14, 15, 16, 17, 18, and 19, to present our findings on the OAM transmission between two identical OAM antennas.

Figure 14 presents the transmission curves obtained when the beam axes of both antennas are aligned, where the rotation angle θ is 0°, with a separation distance of 33 cm between them. The results show that OAM multiplexing can provide 5–8.2 dB cross-mode separation in a communication channel in the frequency range of 6.0–6.1 GHz. In the case where the distance between OAM antennas was increased to 80 cm, the maximum cross-mode level was achieved at 6.07 GHz. At 6.07 GHz, when the transmitted and received OAM modes are the same, the transmission is 11.8 dB greater when compared with the transmission at different OAM modes. Moreover, the results show that OAM multiplexing can provide 8.5–11.8 dB cross-mode separation in a communication channel in the frequency range of 6.05–6.1 GHz when antennas are separated by 80 cm. When Figures 14 and 15 are compared, we note that, although the OAM cross-mode level is less variable within the 6.0–6.1 GHz frequency range for the smaller distance, a higher cross-mode level is achieved for the greater distance. Moreover, both Figures 14 and 15 reveal that as the frequency moves beyond the 5.9–6.2 GHz range, the levels of both co- and cross-mode transmissions increase and converge. At this point, the transmission curves begin to follow the free-space path loss formula, as the nulls at the center of the radiation pattern are removed.

To further explore the system's behavior, the effect of the rotation angle was examined with the OAM antennas placed 33 cm apart. In this scenario, the antennas were rotated in opposite directions on the θ-plane. The transmission curves corresponding to rotation angles of $\theta = 25°$, $\theta = 30°$, and $\theta = 35°$, are shown in Figures 16, 17, and 18.

When we interpreted the results, we found that the imperfections due to the multipath environment and alignment of antennas may have also deteriorated the cross-mode isolation level. Based on our findings, the OAM modes can only be generated within the frequency range of 6–6.2 GHz; this is because the phase shifts are provided with fixed-length series microstrip lines which are designed at 6.0 GHz.

When the transmitted and received OAM mode is the same, as depicted with the red and green curves, the transmission is 5–10 dB higher than the cross-mode transmission (blue). To highlight the relative merits of the proposed design, Table 3 summarizes recent OAM antenna implementations alongside the proposed antenna. The design complexity is qualitatively graded as high, medium, or low, depending on the need for multilayer fabrication, biasing networks, active tuning components, or intricate feed structures. Configurations employing PIN-diode switching, reflectors, or 3D structures are classified as High; substrate-integrated waveguide (SIW) or other moderately intricate topologies are considered Medium, whereas single-layer, series-fed implementations without active components are categorized as Low. Many recent works rely on a higher element count or incorporate additional components such as PIN diodes for mode reconfigurability, SIW slots, or dual-polarized feeds with reflector layers. These approaches' frequency range also appears to be around 6.05–6.15 GHz. As the antennas are rotated in opposite azimuthal directions, they approach the points where the gain is highest, leading to an increase in transmission levels. This increase in transmission comes at the expense of a reduction in cross-mode levels, which is due to the misalignment of the antennas. Misalignment reduces the cross-mode level between the antennas because it disrupts the phase distribution of the vortex beams within the apertures of both the transmitting and receiving antennas.

In the final experiment, we investigated the effect of distance. By increasing the separation to 70 cm, for antennas rotated at $\theta = 30°$, we obtained the transmission curves shown in Figure 19, inevitably increase footprint, fabrication complexity, or operating frequency. By contrast, the proposed antenna achieves dual OAM modes ($l = \pm 1$) at

6 GHz using only four elements in a single-layer, series-fed topology, with a compact aperture of 99×109 mm^2 and a profile of just 0.813 mm. The proposed antenna is not only structurally simple but also easy to fabricate, since the complete feeding and radiating structure is realized on a standard single-layer PCB, eliminating the need for multilayer alignment, biasing networks, or active components.

5. Conclusions

In this paper, we presented the measurement results for the fabricated, series-fed, dual-mode OAM antenna operating at 6 GHz. The measured results include S-parameters, far-field realized gain patterns, phase distributions, and OAM transmission levels for both the same and different OAM modes of the receiving and transmitting antennas. Our results validate that the series-fed, dual-mode OAM antenna, whose elements are connected by fixed-length microstrip lines, can generate OAM modes in the frequency range of 6.0–6.2 GHz. At higher and lower frequencies, the required phase shift, which is 90°, cannot be formed in this design due to the fixed length of the microstrip lines. Finally, the maximum realized gain values are measured as 3.65 dBi for $l = +1$ and 4.8 dBi for $l = -1$ at 6.1 GHz. At 6.1 GHz, the measured OAM spectra obtained at the observation plane exhibit dominant mode purities of 80.6% for $l = +1$ and 73.4% for $l = -1$, confirming successful generation of orthogonal OAM modes.

A comparison of the results presented in Figure 17 versus Figure 19 indicates that as the distance between receiving and transmitting OAM antennas increases, the cross-mode level decreases due to the beam divergence in OAM transmission. These results conclude our experimental assessment of the proposed antenna.

In addition to compact dual-mode radiation, the architecture enables multimode OAM multiplexing, which can increase spectral efficiency. Moreover, one mode may be dedicated to communication while another is exploited for interference suppression, providing robustness without additional hardware complexity.

Nomenclature

OAM orbital angular momentum
VNA vector network analyzer

Data Availability Statement

Data is sharing not applicable to this article as no datasets were generated or analyzed during the current study.

Disclosure

All authors have reviewed and approved the final version of the manuscript for publication.

Conflicts of Interest

The authors declare no conflicts of interest.

Author Contributions

Conceptualization was carried out by I.T. and A.U.; simulations were conducted by A.U.; measurements were performed by I.T. and A.U.; investigation was a joint effort by I.T. and A.U.; original draft preparation was handled by A.U.; writing, including review and editing, was done by A.U. and I.T.

Funding

No funding was received for this manuscript.

Acknowledgments

The authors would like to thank the Sabanci University Nanotechnology Research and Application Center (SUNUM) for providing access to their anechoic chamber for this research.

References

[1] T. D. Drysdale, B. Allen, C. Stevens, S. J. Berry, F. C. Smith, and J. Coon, "How Orbital Angular Momentum Modes Are Boosting the Performance of Radio Links," *IET Microwaves, Antennas & Propagation* 12, no. 10 (2018): 1625–1632, https://doi.org/10.1049/iet-map.2017.0293.

[2] M. Veysi, C. Guclu, F. Capolino, and Y. Rahmat-Samii, "Revisiting Orbital Angular Momentum Beams: Fundamentals, Reflectarray Generation, and Novel Antenna Applications," *IEEE Antennas and Propagation Magazine* 60, no. 2 (2018): 68–81, https://doi.org/10.1109/MAP.2018.2796439.

[3] A. Papathanasopoulos and Y. Rahmat-Samii, "*Fundamentals of Orbital Angular Momentum Beams: Concepts, Antenna Analogies, and Applications*," in *Electromagnetic Vortices: Wave Phenomena and Engineering Applications* (Wiley, 2021), 1–32, https://doi.org/10.1002/9781119662945.ch1.

[4] ITU-R, "Future technology Trends of Terrestrial International Mobile Telecommunications Systems Towards 2030 and Beyond" 2022, https://www.itu.int/dms_pub/itu-r/opb/rep/R-REP-M.2516-2022-PDF-E.pdf. Accessed on 2024-08-31.

[5] L. Allen, M. W. Beijersbergen, R. J. C. Spreeuw, and J. P. Woerdman, "Orbital Angular Momentum of Light and the Transformation of Laguerre-Gaussian Laser Modes," *Physical Review A* 45, no. 11 (1992): 8185–8189, https://doi.org/10.1103/PhysRevA.45.8185.

[6] Z. Guo, Y. Wang, Q. Zheng, C. Yin, Y. Yang, and Y. Gong, "Advances of Research on Antenna Technology of Vortex Electromagnetic Waves," *Journal of Radars* 8, no. 5 (2019): 631–655, https://doi.org/10.12000/JR19091.

[7] R. Chen, H. Zhou, M. Moretti, X. Wang, and J. Li, "Orbital Angular Momentum Waves: Generation, Detection, and Emerging Applications," *IEEE Communications Surveys Tutorials.* 22, no. 2 (2020): 840–868, https://doi.org/10.1109/COMST.2019.2952453.

[8] S. K. Noor, M. N. Mohd Yasin, A. M. Ismail, et al., "A Review of Orbital Angular Momentum Vortex Waves for the Next Generation Wireless Communications," *IEEE Access* 10 (2022): 89465–89484, https://doi.org/10.1109/ACCESS.2022.3197653.

[9] A. Uzun and I. Tekin, "Series-Fed Dual-Mode OAM Antenna at 6 GHz," in *Proceedings of the 2024 IEEE International*

Symposium on Antennas and Propagation and INC/USNC-URSI Radio Science Meeting (AP-S/INC-USNC-URSI) (IEEE, 2024), 2495–2496, https://doi.org/10.1109/AP-S/INC-USNC-URSI52054.2024.10687150.

[10] B. Liu, Y. Cui, and R. Li, "A Broadband Dual-Polarized Dual-OAM-Mode Antenna Array for OAM Communication," *IEEE Antennas and Wireless Propagation Letters* 16 (2017): 744–747, https://doi.org/10.1109/LAWP.2016.2601615.

[11] Y. Y. Wang, Y. X. Du, L. Qin, and B. S. Li, "An Electronically Mode Recon-Figurable Orbital Angular Momentum Array Antenna," *IEEE Access* 6 (2018): 64603–64610, https://doi.org/10.1109/ACCESS.2018.2877782.

[12] Y. Yagi, H. Sasaki, T. Yamada, and D. Lee, "200 Gb/S Wireless Transmission Using Dual-Polarized OAM-MIMO Multiplexing With Uniform Circular Array on 28 GHz Band," *IEEE Antennas and Wireless Propagation Letters* 20, no. 5 (2021): 833–837, https://doi.org/10.1109/LAWP.2021.3065098.

[13] H. Li, L. Kang, F. Wei, Y. M. Cai, and Y. Z. Yin, "A Low-Profile Dual-Polarized Microstrip Antenna Array for Dual-Mode OAM Applications," *IEEE Antennas and Wireless Propagation Letters* 16 (2017): 3022–3025, https://doi.org/10.1109/LAWP.2017.2758520.

[14] M. V. Rao, A. Mawardi Ismail, M. Najib Mohd Yasin, et al., "Novel Switched Mode OAM Beam Generation Using Series-Fed UCA Antenna for AAVs," *IEEE Canadian Journal of Electrical and Computer Engineering* 48, no. 2 (2025): 60–65, https://doi.org/10.1109/ICJECE.2025.3539782.

[15] A. Vedaee and A. Mallahzadeh, "A Single-Layer Series-Fed SIW Slot Array Antenna Generating Two Orbital Angular Momentum Modes," *IEEE Antennas and Wireless Propagation Letters* 22, no. 6 (2023): 1261–1265, https://doi.org/10.1109/LAWP.2023.3239682.

[16] A. Habibi Daronkola, F. Tavakol Hamedani, P. Rezaei, A. Pesarakloo, and S. A. Khatami, "Studying Superposition of Multiple Orbital angular Momentum Modes for Beam Concentration Using Circular Arrays for Long-Range Communication," *International Journal of RF and Microwave Computer-Aided Engineering* 32, no. 11 (2022): e23331, https://doi.org/10.1002/mmce.23331.

[17] M. V. Rao, D. Mondal, J. Malik, M. Kartikeyan, and S. Yuvaraj, "Series-Feed UCA Antenna for Generating Highly Azimuthal Symmetric OAM Beam for Unmanned Aerial Vehicles," *AEU-International Journal of Electronics and Communications* 171 (2023): 154917, https://doi.org/10.1016/j.aeue.2023.154917.

[18] J. Y. Ha and D. W. Seo, "Calculation of Optimum Feed-Line Impedance of Series-Fed Microstrip Antennas Using the Image Parameter Method and Bloch Theory," *Journal of Advanced Marine Engineering and Technology* 47, no. 2 (2023): 78–83, https://doi.org/10.5916/jamet.2023.47.2.78.

[19] CTIA, "Method of Measurement for Radiated RF Power and Receiver Performance" 2019, https://api.ctia.org/wp-content/uploads/2019/04/CTIAOTATestPlan382.pdf. Accessed on 2024-08-28.